PAPER • OPEN ACCESS

Modelling technique and analysis of porous anti-reflective coatings for reducing wide angle reflectance of thin-film solar cells

To cite this article: Timothy Pickering *et al* 2021 *J. Opt.* **23** 025901

View the article online for updates and enhancements.

Modelling technique and analysis of porous anti-reflective coatings for reducing wide angle reflectance of thin-film solar cells

Timothy Pickering[*] ⓘ**, Katie Shanks**[*] ⓘ **and Senthil Sundaram**

Environment and Sustainability Institute, University of Exeter, Penryn Campus, Penryn, Cornwall TR10 9FE, United Kingdom

E-mail: tjp217@exeter.ac.uk and k.shanks2@exeter.ac.uk

CrossMark

Abstract

Bio-inspired anti-reflective (AR) coatings with porous graded refractive index structures are known to considerably reduce the reflectance of light at optical interfaces, however, research is lacking for thin-film cell application. Ray Tracing software coupled with the Effective Medium Theory were used to simulate the reflectance of nanostructured coatings placed above a thin-film system. The most optimal coating was paraboloid-shaped, with 300 nm nipple heights and spacings of 15%. The non-zero refractive index 'step' aids light trapping and energy absorption. This coating reduced reflectance in the $\lambda = 300$–800 nm range by an average of 2.665% and 11.36% at 0° and 80° incident light, respectively, whilst increasing annual energy output by 4.39% and 5.39% for standard UK roof and vertical window tilts, respectively. Significant wide angle reflectance capabilities are demonstrated at specifically $\lambda = 300$ nm and 80° incident light, with a reflectance reduction of 19.192%. There are now many promising manufacturing techniques for these porous nanostructures, such as AR or wavelength filtering coatings for photovoltaics. Further understanding of the exact parameters needed to replicate these nanostructures must be explored to proceed.

Keywords: biomimicry, moth eye, anti-reflective, thin film, photovoltaic, ray trace modelling, nano-structure optical effects

(Some figures may appear in colour only in the online journal)

1. Introduction

Renewable energy systems are an important part of the global effort to tackle the use of fossil fuels that are exacerbating problems such as climate change and global warming. Solar photovoltaics (PV) are an example of such systems that are quickly growing in national and global popularity, with a capacity of 13 447 MW installed in the UK alone, as of July 2020 [1]. This capacity is forecast to increase alongside decreasing costs and higher demand. To meet this demand, solar cell efficiencies will need to increase.

Small changes in solar cell efficiencies can have a huge impact on electricity generation, when considering their global daily use. The efficiency of Silicon solar cells is partly restrained due to their high refractive index [2]. Fresnel reflection loss occurs at the interface between two materials with different refractive indices and is proportional to the refractive

---

[*] Author to whom any correspondence should be addressed.

index gap between each layer. Reducing reflection can be achieved through destructive interference or a refractive index gradient. These changes in solar cell design improve the cost-effectiveness of solar modules.

Anti-reflective (AR) coatings with gradient refractive index profiles can increase the light absorption and power output of solar cells [3, 4]. These nanopatterns were biologically inspired by structural observations of moth-eyes and other insects. The compound eyes of moths were found to reflect little or no light, regardless of the lights angle of incidence (AOI) [5]. The intricate design of these biological structures have evolved over millions of years through natural selection selecting optimal characteristics for a species' survival [6]. Scientific advancements on engineering applications can therefore be made through imitating nature with bio-inspired creations, for example, in the case of AR coatings. Sections 1.1.1 and 1.1.2 detail the current understanding of the moth-eye and Glass-wing Cicada nanopatterns, whilst section 1.2 briefly analyses the literature surrounding AR coatings and those applied to thin-film solar cells.

This study focuses on the application potential for thin-film solar cells, as they are the second most marketed PV device after crystalline-PV, as well as being lightweight, cost-effective and flexible. Most solar panels are fixed in one position and there is increasing advancement towards building integration. This has resulted in greater demand for wider acceptance angles to provide more power throughout the day, especially during the Sun's low-angled winter months. AR coatings are a potential solution to this demand.

Porous AR coatings have been previously researched, especially porous Si because of its solar energy application [7–10], but the optimum modelling and manufacturing methods are still to be agreed. Si has been explored in all types of AR coatings, starting from porous Si on solar cells to moth-eye inspired structures. However, porous AR coatings for thin-film solar technologies are less thoroughly researched and such graded refractive indices could be applied to the glass substrate or between the glass and solar cell layers (discussed further in section 4.4).

Optical analysis simulations during the design phase of any solar device can remove the need for expensive rework later. This emphasises the importance of Ray Tracing software in accurately modelling the scattering of light of these coatings [11], but it would be most beneficial if the final manufactured samples performance was represented, accounting for flaws and limitations. It is difficult to isolate optical properties within natural nanostructures whilst measuring the refractive index and reflectance values, hence optical modelling is an essential tool in understanding these parameters (see table 1, discussed in section 4). One of the most practical fabrication approach for nanostructured AR coatings is to reduce the packing density of the films. However, this affects the mechanical strength of the coatings and raises durability issues [7].

This novel study isolates the effects of porosity on the refractive index and hence the reflectance reduction, using graded refractive index layers with graded porosities (see figure 2, discussed in section 3). However, the porosities are

based on the ratios of material to air in the moth-eye nanopatterns, to broaden understanding of these nanoscaled structures properties. Previous research sometimes omits wider angles of incidence greater than 70° and can lack modelled predictions of PV annual energy increase due to the developed AR coating (especially thin-film AR coatings), which are further novelties of this work [4]. This study therefore analyses the effects of AOI up to 80° and includes a comparison for the estimated annual energy production using PVSyst, from non-coated to AR coated thin-film cells. Reflection spectra are obtained for designed nanostructure geometries on amorphous silicon (a-Si) thin-film solar cells, using a Ray Tracing modelling approach. The aim is to simulate nanopattern AR structures using novel geometries, to reduce reflectance and considerably increase thin-film cell efficiency and performance over wide angles of incidence.

An important talking point is how this data could be used in the wider narrative. AR nanostructures can be applied to monitors, optical devices and solar cells [7, 12]. Edgehog Technology [13] is an example of commercialised nanostructure AR coating technology which can provide glass surfaces with 99.8% light transmittance, proving the commercial viability of AR coatings at a relatively high price. It is crucial that these nanostructures can be effectively constructed at a low cost and with large scalability. This is a challenge for the increasing use of biomimicry in all nano-scale applications, including AR coatings.

1.1. The biomimicry challenge for PV

1.1.1. Glass-wing Cicada. The transparent wings of this butterfly have low haze and reflectance properties over the whole visible spectral range, even for angles of incidence of 80° [14]. A large number of high aspect ratio cone-shaped nanopillars are located on the transparent region. The irregularly arranged nanopillars are distributed in the areas of these bristles with heights between 160 and 200 nm, diameters of ∼160 nm and spacing of ∼180 nm [15]. A low specular reflectance of 2% was found at a wavelength range from 390 to 700 nm with an incident angle of 65°, increasing to ∼5% for 80°. These random nanopillars possess omnidirectional AR performance and hydrophobic characteristics. Given the humid environment it resides in, its hydrophobic property allows for a lightweight state to be maintained. The nanopillar arrays enhance absorption/transmittance through optical impedance matching, creating effective camouflage [15]. Siddique *et al* [14], performed an optical analysis on this butterfly, finding that the omnidirectionality is caused by the nanopillars random height distribution. Optimising the distribution and shape of these structures can be used to create AR surfaces that function at a wide range of wavelengths and angles of incidence. Replicating these nanopatterns show great potential for greatly reducing reflectance at wide angles, however, scientists have only just begun to understand these nanostructures and how to replicate their properties.

If the nanopillar height varies across the area of such structures, then does this mean the porosity and hence refractive index also varies following the effective medium theory
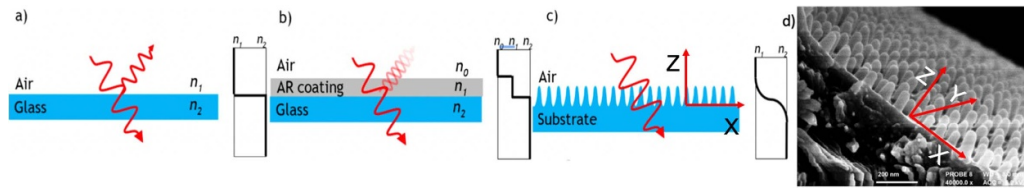
Figure 1. (a) Fresnel reflection. (b) Single layer AR coating. (c) AR nanostructure technology. (d) Moth-eye nanopattern structures, with a 200 nm scale bar [21].

(EMT)? Does the shape and frequency of these structures have a stronger effect than the overall porosity and effective refractive index? This is a complex investigation, initially requiring the isolation of the porosity effects on the graded refractive index for glass-topped thin-film solar cells.

1.1.2. Moth-eyes. Moth-eye nanopatterns were used as the original inspiration for AR coatings on solar cells by increasing absorption. They are already widely explored and there is a robust understanding of their mechanics, but perhaps this biomimicry has more to offer in terms of wide angle reflectance reduction. This potential to decrease reflectance at higher angles of incidence could improve morning and evening electricity generation from solar cells [16].

First discovered by Bernhard *et al* [17], moth-eyes are made up of corneal nipples structures (figure 1(d)), that create a refractive index gradient transition between air and the facet lens material, due to their small (nm) size with respect to the wavelength of light. They reduce the reflectance on a smooth facet lens surface from ∼4%–1% [5].

Moths are nocturnal which could explain the need for reflectance reduction on the eyes caused by these nipples [18]. Moths are likely ancestral to butterflies, suggesting that the reduced nipple size in most butterflies indicates a diminishing trait [5]. Moths are inactive in the day and vulnerable to predation, therefore the nipples act to reduce reflectance and the incurred visibility, acting as camouflage. However, direct empirical evidence of this effect has not yet been obtained, with further research suggesting that these arrays are common amongst both diurnal and nocturnal insects [5, 19]. Other theories for these nipple shapes include improved vision and light sensitivity in low light conditions by reducing light reflection and reduction of water wettability by creating superhydrophobic surfaces [20].

Spalding *et al* [21], further analysed the understanding of functional roles for these corneal nipple structures. This included an explanation of why moths are attracted to UV light. Using Ray Tracing methods, they observed that these structures are missing from some moths and butterflies, with differences between nocturnal and diurnal species. The theory that moth-eyes reduce reflectance to avoid predation was contradicted by the varying reflectance results at different wavelengths found in Spalding *et al*'s [21] work, with greater absorption at UV wavelengths. Additionally, the effective refractive index at the top of the moth-eye nipples is close to that of water, which in theory, allows for minimal vision distortion when droplets 'sit' on the nipple dome tops, due to

rain. Similarly the nanopatterns were found to reduce adhesion from the decrease in real contact area between contaminating particles and the eye surface.

1.2. The effect of AR structures on solar cells

1.2.1. AR coatings. Researchers have investigated the effects of AR coatings alone, without a solar PV system in place. Stavenga *et al* [5], collected results using several nanostructure geometries, concluding that the largest reduction in reflectance occurs for paraboloid nipples with 0% nipple spacing relative to its height, at <1% reflectance for each wavelength in the range 300–700 nm. Yoshida *et al* [22], investigated the effect of nipple arrays on the wings of a Hawkmoth. The reflectance was ∼1.5% with nipples, but ∼4% after they were removed. Yoshida *et al* [22], suggested that the precise shape of the nipples is unimportant for the reflectance reduction, but height is a key factor. Boden and Bagnall [23], investigated reflections from AR coatings over a 24 h period at varying angles of incidence. Nipples at heights of 500 nm were the most effective in this study, with the percentage of photons reflected over a day dropping to 25% of the value for an optimised single layer AR coating, resulting in an energy production rise of 12%.

AR structures on organic solar cells have been examined briefly in the literature [24, 25], whilst inorganic cells are more comprehensively covered [2, 26–29].

1.2.2. AR coatings on thin-film solar cells. AR coatings on thin-film solar cells are only briefly investigated in the literature. Siddique *et al* [30], created a randomly ordered nanostructure AR coating for thin-film cells, based on Pachliopta Aristolochiae black butterfly wings. Their simulations found a reflection decrease of 10% at normally incident light, due to high efficiency in light in-coupling and trapping. A study by Jang *et al* [4], presented an average reflectance of <10% at wavelengths of 400–800 nm in the incident angle range of 0°–50°. Jang *et al* [4], fabricated very simple and low cost graded refractive index structures between the Indium tin oxide (ITO) and a-Si layers of a thin-film cell, providing efficient wideangle AR properties. This addressed the refractive index jump between these layers, which few have investigated. Jang *et al* [4], found that the average reflectance of an a-Si thin-film solar cell structure with a graded refractive index, is reduced by 54% at normal incidence due to the effective refractive index matching between ITO and a-Si. There is yet to be studies indicating the full potential of many AR layers within thin-film cells

(e.g. the use of both external and internal AR coatings), something which is explored in this research. This will include the combination of Jang *et al*'s [4], AR coating between the ITO and a-Si layers, as well as an optimised wide-angle AR coating between the glass and ITO layers.

2. Theoretical background and physics

2.1. Anti-reflection theory

$$R = \left(\frac{n_1 - n_2}{n_1 + n_2} \right)^2 \tag{1}$$

where 'R' is the reflectance and '$n_{1,2}$' is the refractive index of medium 1 and 2, respectively.

Equation (1) is the reduced Fresnel equation that calculates the normal reflectance from incident light on a flat interface between different materials, created due to the sudden jump in refractive index between the two mediums (figure 1(a)). The Fresnel equations can be used in Ray Tracing calculations to designate flux and direction to transmitted and reflected rays.

For light moving from air ($n_1 = \sim 1$) to a glass layer ($n_2 = \sim 1.5$), reflectance at normal incidence is $\sim 4\%$. To reduce this, quarter wavelength AR single/double/multiple surfaces can be used where the refractive index and thickness cause destructive interference in the waves reflected at each interface (figure 1(b)). These surfaces are the least complicated AR coatings and can only be optimised for a single wavelength and AOI, due to their reliance on interference [16].

Edgehog [13], amongst other companies, have therefore created nanostructure AR technology. This can significantly reduce the reflectance, by removing the jumps in refractive index at the interface by gradually increasing the refractive index between the two materials, thus creating a smooth gradient. These effective refractive indices can be designed with texturing surfaces on a nano-scale, smaller than the wavelength of light (figure 1(c)).

Figure 1(d), demonstrates SEM images of moth-eye nipple structures [21]. The moth-eye facet lenses are approximately hemispherical in shape and the convex outer surface of these facet lenses consists of corneal nipples in a regular, hexagonal lattice.

It's crucial to note that light interacts differently on structures with dimensions less than its wavelength [7]. Light interacts with the rough surface wholly as the wavelength of light is higher than the dimension of the structure and as if the surface has a gradient refractive index, light rays tend to bend progressively. If the same dimensional constraints are applied to the spacing and depth between nanostructures in textured or grooved surfaces, light rays get trapped in the crevices resulting in multiple internal reflections. Nanostructures are therefore 'seen' as a medium of varying refractive index.

2.2. Effective medium theory

Han and Chang [16], reviewed progress in the modelling of AR sub-wavelength structures, covering techniques including:

(a) **[Time-based]** Finite-difference time-domain (FDTD)
   This method allows for multiple wavelengths per simulation and is capable of modelling arbitrary shapes. It is computationally intensive, relies on an effective media approximation for more complicated geometry and is capable of describing the geometry of nanostructures.
(b) **[Frequency-based]** Transfer matrix method (TMM)
   This method is only appropriate for very simple coatings.

All of these rigid numerical methods were found to accurately predict reflections of AR sub-wavelength structures, as well as being capable of simulating non-zero angles of incidence. Each of these methods has benefits and limitations, but ultimately the EMT coupled with Ray Tracing was selected for these initial investigations to isolate the effects of porosity. EMT is not effective for many direct measurements but is accurate for calculating the effective refractive index. These specific optical and EMT methods were also chosen as they have previously been used to analyse moth-eye nanopatterns in the literature [5, 21]. Stavenga *et al* [5], used this method and obtained results that matched experimental measurements of moth-eyes.

There are very few materials with refractive indices between glass and air, resulting in large reflections from this big jump in refractive index. Therefore, sub-wavelength geometries are currently the most accessible method to produce a smooth effective refractive index gradient between the two interface materials which reduces reflections. When the designed AR geometries are smaller than the wavelength of light, the effective refractive index values can be found using the EMT equations. Unlike the other modelling techniques, the EMT does not directly determine reflectance of an AR coating, and instead focuses on the layers of a medium and its porosity. It works by accurately calculating the effective refractive indices of nanostructure geometries based on the volume fill factor of the material to air [16]. It therefore simulates mediums and not actual structures. The effective refractive index gradient values were obtained by dividing the nipple height into layers where thickness = $\frac{\text{nipple height}}{\text{layer number}}$. The stack of layers can then be treated as a layered optical system that represents the entire modelled nipple surface.

Further applications of the EMT include the design of a broadband waveguide bend [31, 32]. A gradient index medium can be implemented by varying the thickness of the guiding layer, or by using subwavelength grating structures. In this research by Badri and Gilarlue [32], the effective refractive index of a layered structure depends on the alignment of layers with respect to the electric field direction, whereby the lens is realised by changing the filling ratio of silicon rods.

Figures 1(c) and 2, show how the EMT works in terms of replicating the nipple structures with an effective refractive index gradient. Ray Tracing uses the EMT by simulating light interacting as a refracting wave with respect to the nanostructures.

There are three commonly used EMT theories which all assume roughly spherical sub-wavelength grains [16]. Bruggeman's [33] EMT was used for this study as it is the most widely known theory and unlike the Maxwell–Garnett
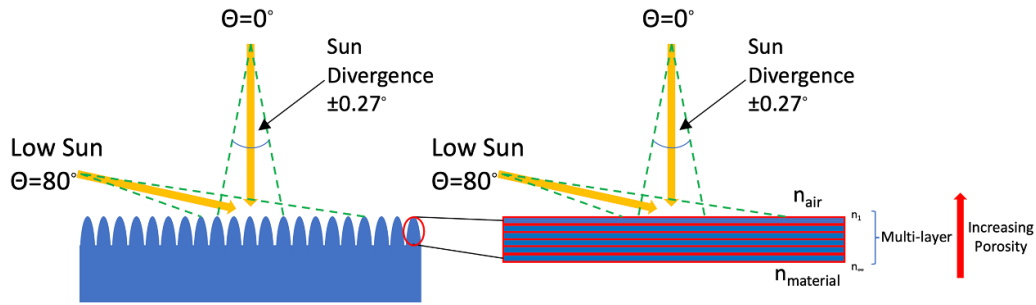
Figure 2. The simulated layered nanostructure, consisting of multiple effective refractive index 'steps'. These refractive index 'steps' are later depicted by the *x*-axis in figure 6(b). Here, the actual nipple geometries are further described.

formula, it can give rise to a critical threshold and it can be generalised to include any number of components [34]. This method is used for more than 2 materials, where the effective refractive indices align between the materials (equation (2)).

$$\sum_{i=1}^{k} f_i \left[\frac{(n_1^2 - n_e^2)}{(n_1^2 + 2n_e^2)} \right] = 0 \tag{2}$$

where 'k' is the number of constituents in a homogeneous mixture, 'n_e' is the effective refractive index, '$n_{1,2}$' is the refractive index of medium 1 and the AR coating material, respectively, and '$f_{1,2}$' is the fill factor of materials 1 and 2, respectively.

There are several commonly reported simple mathematical gradient index profiles reported by Han and Chang [16], whereby the linear profile was chosen for this research (equation (3)).

$$n_e = n_1 + (n_2 - n_1)t \tag{3}$$

where 't' is the distance from the substrate in the nanostructure region, 'n_e' is the effective refractive index and '$n_{1,2}$' is the refractive index of medium 1 and the AR coating material, respectively.

The EMT only estimates these values via varying porosity and does not take into account corneal nipple shape. However, the FDTD method takes into account shape but is not required for the porosity investigations here. Future work will compare these two methods of replicating the corneal nipple geometries, via shape and density, to aid understanding of which nano-properties have the 'dominating' AR effects and/or specific wavelength filtering.

3. Simulation methods

3.1. Script functionality experiment

Firstly a reconstruction of past simulative works was made [5], using the same geometry equations and nipple parameters. The nipple shapes are expressed in terms their respective equations, and assumed to be hexagon-based, justified by SEM imaging [5]. The *z*-axis was taken to be perpendicular to the corneal surface, with the nipple troughs at $z = 0$ and peaks at $z = h$ (figure 1(c)). Equations (4) and (5) represent the relative

amplitude and distance values required for the geometry equations:

$$z^* = \frac{z}{h} \tag{4}$$

where 'z^*' is the relative amplitude, 'z' is the *z*-coordinate and 'h' is the peak amplitude value.

$$r^* = \frac{r}{d} \tag{5}$$

where 'r^*' is the relative distance, 'r' is the distance to the nipple axis and 'd' is the distance of 2 adjacent nipples.

The replicated cone nipple geometry is represented mathematically by equation (6). A plane at z^* contains a fraction of corneal material, shown by equation (7).

$$z^* = 1 - \frac{r^*}{p} \tag{6}$$

where 'z^*' is the relative amplitude, 'r^*' is the relative distance and 'p' is the nipple width parameter.

$$f(z^*) = \frac{\pi r^2}{A_n} = \frac{2\pi r^{*2}}{\sqrt{3}} \tag{7}$$

where '$f(z^*)$' is the fraction of corneal material at plane 'z^*', 'r' is the distance to the nipple axis and 'A' is the area.

Figure 2 describes the modelling architecture used to simulate the nipple shapes using a smooth refractive index gradient using multiple nm-scale layers. In these simulations, the facet lens medium refractive index was taken to be 1.52 [35], as for this value, the effective refractive index layer values are well approximated by equation (8).

$$n_e(z^*) = [f(z^*)n_c^{\frac{2}{3}} + (1 - f(z^*))]^{\frac{3}{2}} \tag{8}$$

$$n_e(z^*) = f(z^*)n_c + (1 - f(z^*)) \tag{9}$$

where '$n_e(z^*)$' is the effective refractive index at plane 'z^*', '$f(z^*)$' is the fraction of corneal material at plane z^* and 'n_c' is the facet lens medium refractive index.

This 1.52 refractive index is taken from interference microscopy results of moth corneal lens samples [35]. This obtains
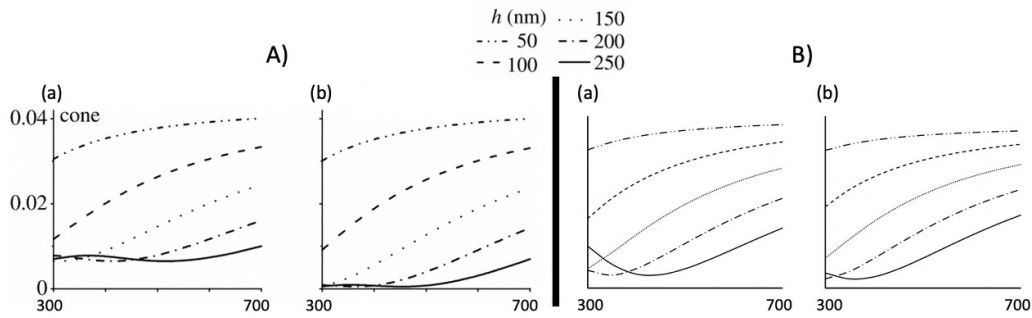
Figure 3. Modelled wavelength vs reflectance spectra for (a) 25% spacing and (b) 0% spacing. Data from Stavenga *et al* [5], is on the left (A), whilst the replica data from this research is on the right (B).

values that only slightly deviate from those extracted from the simple weighting formula shown by equation (9). For paraboloid-shaped nipples, $f(z^*)$ and $n_e(z^*)$ are therefore approximately a linear function of z^*. When $z^* < 0$, the refractive index is that of the facet lens medium (1.52). When $z^* > 1$ the refractive index is that of air ($\sim$1). The refractive index for $0 < z^* < 1$ follows from the EMT.

Stavenga *et al* [5], ran simulations to generate reflectance spectra of several geometries for normally incident light at five different nipple heights (50 nm, 100 nm, 150 nm, 200 nm and 250 nm) and two spacings of $p = 0.53$ (0%) and $p = 0.4$ (25%). Figure 3 shows the wavelength vs reflectance spectra found by Stavenga *et al* [5], using the TMM on the cone geometry (figure 3(A)) as well as the replica simulations performed using Ray Tracing (figure 3(B)). It is evident from these results that the taller the nipples, the lower the reflectance of light. Interestingly, the Ray Tracing layer limitation has a significant effect on the resulting reflectance spectra of the higher nipple heights (>200 nm).

It is clear that the model used in this research is accurate for lower nipple heights when comparing with the work by Stavenga *et al* [5] (figure 3). This highlights the potential benefits of fabricating smaller nipples for AR coatings. Taller nipple sizes have more associated errors using this model, due to the associated layers limitation. This results in higher reflection values from this research than those simulated by Stavenga *et al* [5]. For this reason, this model is not accurate in representing the real moth-eye structure at higher nipple heights, due to the inaccuracies in simulating the gradual refractive index gradient.

However, it could be accurate for synthetic AR coatings for taller nipple heights due to limitations in manufacturing steep, smooth nanostructure slopes without high expense [36]. It is possible that this model is negatively bias towards taller nipples and is more accurate for determining the realistic reflection, due to the graded refractive index 'steps' inherent to manufacturing and most evident from flaws or 'bumps' during fabrication [12]. This is taken as a positive, as it means that when these nanostructures are fabricated, the results of the taller nipples will accurately represent the manufactured sample and could potentially be even more impressive than originally simulated (if high quality, expensive manufacturing is adopted). Going forward, the core results from this research

are comparative in nature, negating some of the modelling inaccuracies.

3.2. Importance of nipple layers

The next experiment ascertained whether or not the number of layers used in the EMT had an affect on the reflectance results. A cone geometry was chosen at a height of 200 nm with a nipple width parameter of 0.4 p (25%), with light travelling from air into a facet lens medium with a refractive index of 1.52. The simulation was performed with 52, 60, 70, 80, 93 and 97 layers. The number of media allowed in the software was limited, thus restricting the total number of layers that could be investigated in this experiment to 97. As discussed above, this limits the accuracy of replicating actual moth-eye reflectance [5], but equally this could be a similar layering limitation to the actual fabrication of these structures, which is more useful to consider. The values for 0 layers represent the reflectance of light going from air directly into the facet lens medium (1–1.52), without a nanostructure present. The greater the number of layers, the lower the reflectance, with figure 4(a), displaying a considerable drop in reflectance between 52 and 97 layers at $\lambda = 500$ nm.

3.3. Importance of nipple spacing

This experiment was carried out to gauge how nipple spacing affected the reflectance spectra. It was decided that increments of 5% spacing would be used from 0% (nipples touch bases) until 50%, where the nipple spacing is calculated as a percentage of the nipple height. The nipple shape contracts as the spacing value increases, changing the fraction ratio of air:material. A 200 nm high cone geometry with 97 layers was selected for this experiment.

Figure 4(b), demonstrates how the reflectance changes for the 300–700 nm wavelength range, with various nipple spacings. The pattern is clear, whereby the reflectance decreases from 0% to 15% (black) and then starts to increase again from 20% to 50% (red). The route from 0% to 50% spacing is depicted by the arrows on the graph. It was concluded that a spacing of 15% of the nipple height has the lowest reflectance values over the entire wavelength range, for the case of normal incident light.
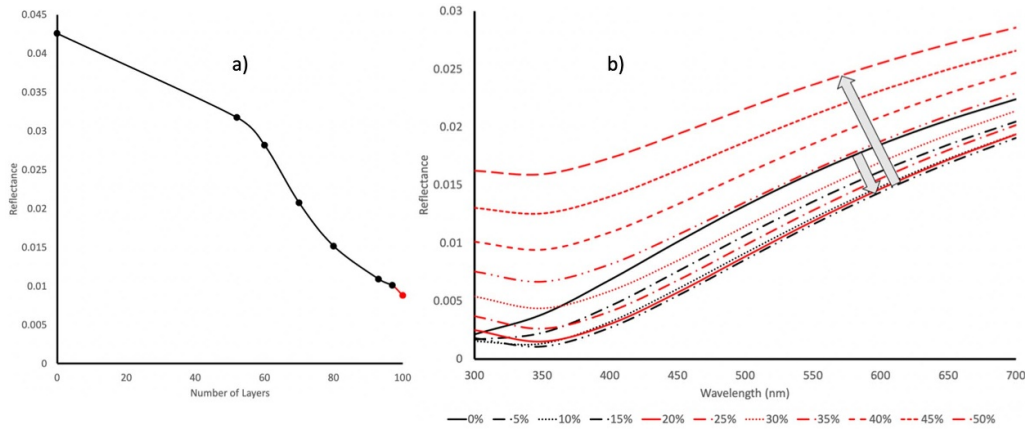
Figure 4. (a) Reflectance vs number of layers for $\lambda = 500$ nm, for 200 nm cone-shaped nipples at $p = 0.4$ (25% spacing). Here, the value marked in red represents the equivalent data point from Stavenga *et al* [5]. (b) Reflectance vs wavelength graph for 200 nm cone-shaped nipples with 97 layers and a variation in the nipple % spacing.
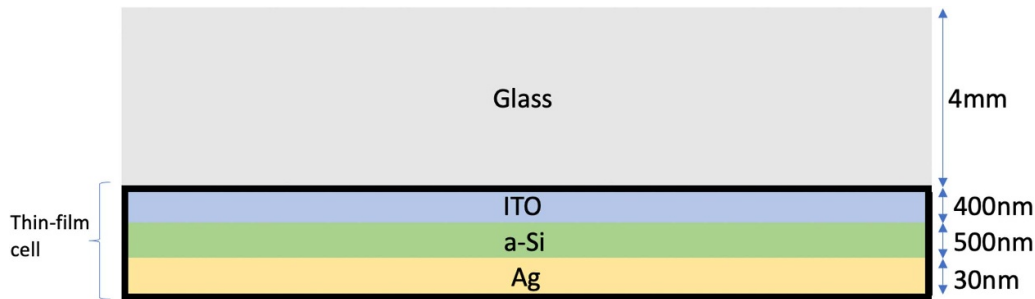
Figure 5. Amorphous silicon thin-film solar cell layered structure.

Table 1. Summary of the reflection simulation parameters. As porosity is the research focus, the '%' units are much more useful when describing nipple spacing.

Parameter	Value
Nipple layers	97
Nipple spacing	15% of the nipple height
Nipple material refractive index	1.52
Divergence of light	0.27° (sunlight)
Simulation AOI range	0°–80°
Simulation nipple height range	200–300 nm
Simulation geometries	Cone/paraboloid
Simulation wavelengths	300–800 nm
Resultant refractive index gradient	Figure 6(b)

4. Results and discussion

Simulations were carried out with the moth-eye nanostructures (represented by their porosity and refractive index layers) placed atop the thin-film glass layer (between air and glass), to replicate how light interacts with the different refractive indices of this system (figure 5). The objective is to increase the light that reaches the absorptive a-Si layer, thus increasing the absorption efficiency of the thin-film cells over a large range of wavelengths and angles of incidence. Simulation parameters are summarised in table 1.

This basic design was adapted from Jang *et al* [4], where a similar setup expressed the thicknesses of each layer required for this kind of a-Si thin-film cell. The thickness for cubic profiles of the ITO, a-Si and Ag layers are 400, 500 and 30 nm, respectively. These thicknesses allow the ITO layer to have minimal reflectance and the a-Si layer to have a high efficiency of absorption.

The refractive indices were collected for each of the different layers used in the simulation for varying wavelengths (table 2). Values for the refractive index of a-Si could not be determined using a database, thus the literature was used to determine average values for each wavelength [39–41].

Small changes in the graded refractive index layers have little effect on reflectance. However, this research found that for the a-Si thin-film system, (figure 5) the optimum geometry for these investigations was achieved by a parabolic-shaped nanostructure (in agreeance with Stavenga *et al* [5]) with 300 nm nipple height (figure 3) and 15% nipple spacing (represented by the refractive index gradient in figure 6(b)). This follows the relationship between increasing height and decreasing reflectance found in previous research [5, 22, 43], as well as that analysed in section 3.1. The 300 nm height was selected as optimum in this research as greater heights simulated showed insignificant changes to reflection capabilities at all wavelengths. This may be due to the layers limitation which perhaps begins to dominate, however, as previously suggested, this may be an accurate bias for manufacturing

Table 2. Database refractive index values for the thin-film cell layers including Glass-BK7 [37], ITO [38], a-Si [39–41] and Ag [42].

Wavelength (nm)	Refractive index			
	Glass-BK7	ITO	a-Si	Ag
300	1.5528	2.3434	3.6000	1.3453
350	1.5392	2.1342	4.5000	0.1144
400	1.5308	2.0355	4.7600	0.0500
450	1.5253	1.9685	4.7800	0.0400
500	1.5214	1.9136	4.5800	0.0500
550	1.5185	1.8636	4.4300	0.0596
600	1.5163	1.8149	4.2800	0.0552
650	1.5145	1.7653	4.1300	0.0522
700	1.5131	1.7136	4.0500	0.0410
750	1.5118	1.6588	3.9300	0.0312
800	1.5108	1.5999	3.8500	0.0368

limitations, supported by previous research which has shown that nipple heights > 300 nm would cause fabrication difficulties [23]. Following the theory introduced previously, it might have been expected that a spacing of 0% should have the lowest reflectance due to its more gradual refractive index gradient and final effective refractive index of ∼1.5 at the start of the solid glass layer. However, the 15% spacing was optimal, perhaps due to internal light trapping effects. In theory, having some small controlled 'step' in refractive index will allow total internal reflection to aid light trapping, whereas a completely smooth refractive index gradient at this end layer into solid glass would allow small portions of reflected light to escape very easily even though it would be travelling with a widened angle (due to reflection from the a-Si layer).

The effective refractive index values of the paraboloid geometry decrease linearly, as shown in figure 6, with this geometry described mathematically by equation (10) (physical architecture described by figure 2).

$$z^* = 1 - \left(\frac{r^*}{p} \right)^2 \qquad (10)$$

where 'z^*' is the relative amplitude, 'r^*' is the relative distance and 'p' is the nipple width parameter.

Figure 6 demonstrates how altering the nipple spacing affects the shape of the nipples and their effective refractive index gradients. Figure 6(a) shows the amplitude of the nipples relative to the peak value (z^*), shown as a function of the distance relative to the distance of two adjacent nipples (r^*). Figure 6(b) shows the effective refractive index values at relative amplitudes, z^*. The percentage spacing is taken relative to the height of the nipples used in each simulation. Figure 6(b) also shows how the paraboloid geometry has a linear relationship to the effective refractive index—something which could explain why it performs optimally compared to other geometries.

- When $p = 0.53$ the base area = hexagonal lattice unit cell. Here, paraboloid nipples give a near linear refractive index gradient.
- When $p = 0.455$ the base area < hexagonal lattice unit cell. This causes the effective refractive index value to jump from 1.38 to 1.51 at $z^* = 0$, as shown in figure 6.

4.1. Key observations and assumptions

- **Nipple height**—The taller the nipple geometries (**300 nm**), the smaller the reflection values at most wavelengths.
- **Nipple layers**—The greater the number of layers (**97**), the smaller the reflections at all wavelengths.
- **Nipple spacing**—The nipple spacing of **15%** relative to the height produced the lowest reflection values at all wavelengths.
- **Light trapping**—A small refractive index 'step' is required to aid total internal reflections and hence light trapping, which improves total energy absorption.

See table 1 for further simulation parameters.

4.2. Wide angle analysis

Figure 7 depicts the reflectance vs wavelength graphs for each AOI, comparing the paraboloid geometry on top of the thin-film system, to the thin-film system without a nanostructure in place. There are clearly large reductions in reflection across the whole wavelength spectrum for each of the angles of incidence, with reductions increasing as the AOI is increased. For stationary solar cells like this one, the behaviour of the coating at a variety of angles of incidence is vital.

Table 3 and figure 8(A), show the average reflection reduction values for each AOI, as well as the associated minimum and maximum values. The largest reflection reduction is 19.192% for $\lambda = 300$ nm and an AOI of 80°. The lowest reflection reduction is 2.06% for $\lambda = 500$ nm and an AOI of 20°. Each wavelengths reduction remains very similar between 0° and 30°. Average percentage reduction for each AOI are also listed in table 3. It can be seen that the percentage reflection reductions generally decrease until 20° before increasing exponentially towards 80°. It is clear that there are greater reflectance reductions towards the visible region of the electromagnetic spectrum, allowing for greater absorption of these 'useful' wavelengths. There are smaller percentage reductions at the infrared region of the spectrum, which is an important characteristic as these wavelengths heat the cell and can cause a decrease in efficiency.

These results are in agreeance with similar work by Jang *et al* [4], who fabricated AR coatings between the ITO and a-Si layers of a thin-film cells and found an average reflectance of <10% at wavelengths of 400–800 nm in the incident angle range of 0°–50°. Research by Siddique *et al* [30], also supports these results, where AR coatings based on black butterfly
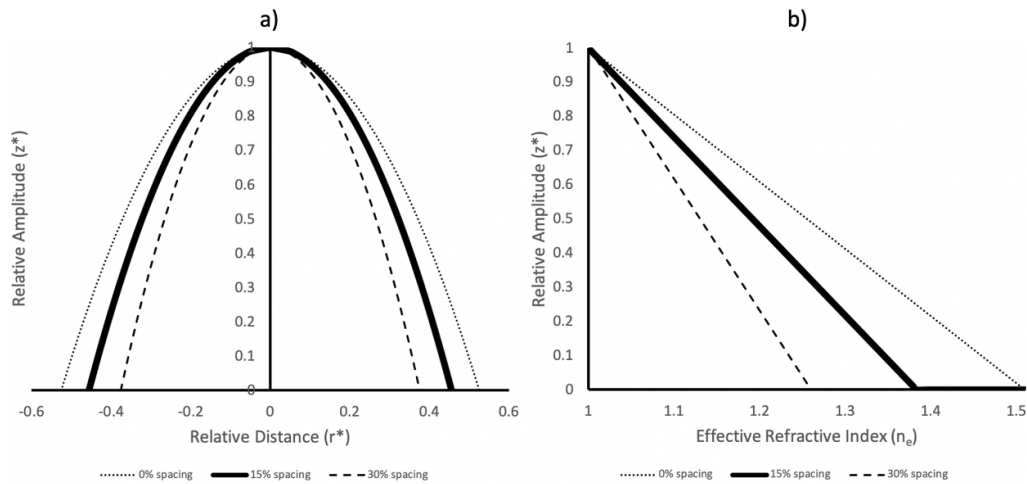
Figure 6. (a) Relative distance vs relative amplitude, demonstrating the shape of the optimum paraboloid geometry at 15% spacing, compared to 0% and 30% spacing. (b) Effective refractive index vs relative amplitude of the optimum paraboloid geometry at 15% spacing, compared to 0% and 30% spacing.

wings were simulated for thin-film cells, finding a reflection decrease of 10% at normally incident light.

4.3. Individual wavelength analysis

Figure 8(B), shows how the reflectance for 500 nm light increases with greater AOI. This compares a system with the glass and the thin-film cell only, to the system with the paraboloid 300 nm, 0.455 p (15% spacing) nanostructure placed on top, to the system with just the paraboloid nanostructure. It also highlights how the increase in nipple height decreases the reflectance of the nanostructure without the glass or thin-film cell. The incident angles from 0°–50° are known to be very important for practical solar cell applications. After 50° in figure 8(B), the reflectance for the full system with the AR coating begins to exponentially increase, thus supporting this statement. The percentage reduction decreases from 2.160% at 0° to 2.061% at 20°, before increasing exponentially to 11.557% reduction at 80°. This shows the wide angle potential of this nanopattern structure. This is particularly promising for enhancing electricity generation when the Sun is low in the sky in the morning and evenings.

4.4. Multiple AR coatings

The large differences between the system with and without the AR coating are very significant, but it is clear from the remaining gap underneath the 'paraboloid, glass and cell' curve in figure 8(B), that further reductions could be made. This could be achieved through nanopatterns placed between the ITO and a-Si layers, such as those designed by Jang *et al* [4]. In terms of fabrication, similar structures could be used for each nanopattern in front of and behind the glass with no air gaps, with each layer finely slotting into place over each other on a nanoscale.

Table 4 analyses the average reflectance between the 300–800 nm wavelength range, for the thin-film system in three scenarios:
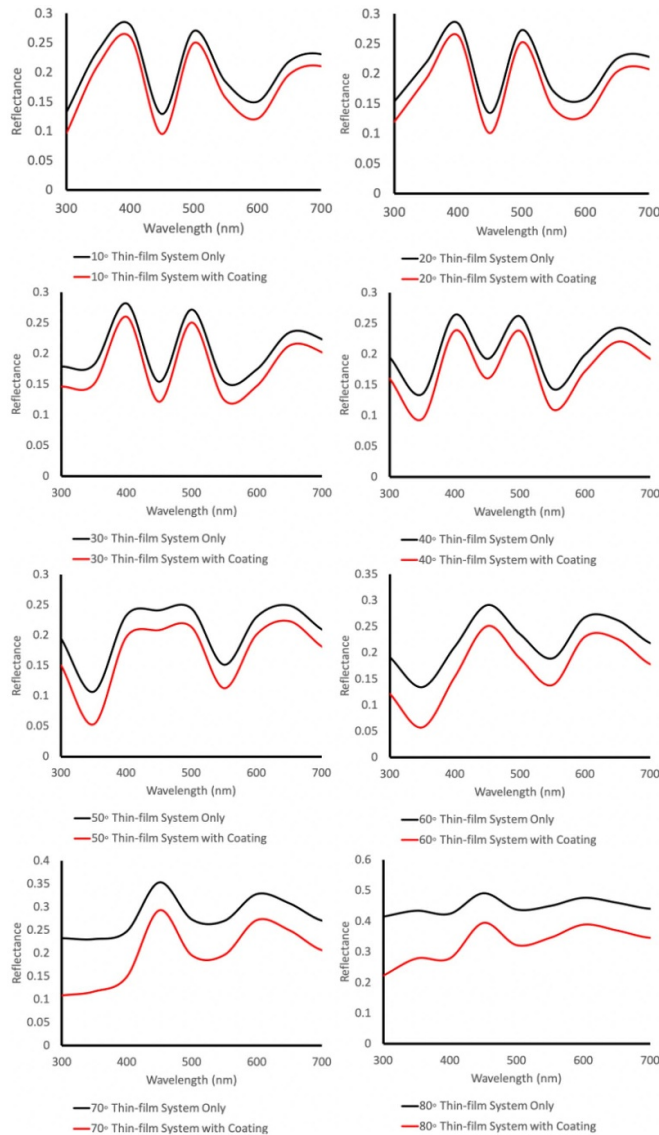
(a) No AR coating
(b) One (**external**) AR coating—this study's optimum coating set between the glass and a-Si layers
(c) Two (**external and internal**) AR coatings—this study's optimum coating set between the glass and a-Si layers (paraboloid geometry, 300 nm height and 15% spacing—summarised in table 1), combined with Jang *et al*'s [4] AR coating set between the a-Si and ITO layers.

The average reflectance from the a-Si thin-film system using both coatings was found to be reduced by 12.4% for normally incident light, compared to 17.2% for light incident at an 80° angle, due to the graded effective refractive index matching between the glass, a-Si and ITO layers.

4.5. Annual energy production

Figure 9 compares how the annual system production of a 10 kW$_p$ a-Si thin-film system increases at a 42° (standard roof) and 90° (window) tilt, for the three scenarios described. This demonstrates an annual energy increase of 4.39% and 5.39% for 42° and 90° tilts, respectively, with the use of this study's optimum coating. When this coating is used alongside another created by Jang *et al* [4] set between the a-Si and ITO layers, the annual energy production can be seen to increase by 13.38% and 14.21% for the 42° and 90° tilts, respectively. These improvements in performance are in line with the greatly reduced wide angle reflections shown in table 4, offering year-round positive implications for energy generation.

Cadmium Telluride thin-film solar cells were also simulated on PVSyst, using the same reflectance data extracted for the a-Si system in this study. Similar annual production percentage increases were found, with 4.34% (42° tilt) and 13.05% (90° tilt) increase for one coating, compared to 5.41% (42° tilt) and 14.19% (90° tilt) for two coatings.

Figure 7. Reflectance vs wavelength values for varying angles of incidence with the paraboloid geometry on top of the thin-film system, with 300 nm nipple heights and a spacing of 15%, compared to the thin-film system only.

Table 3. Min, max and average percentage reflection reductions for each AOI value from $\lambda = 300$–800 nm, using the optimum paraboloid 300 nm, 15% spacing geometry.

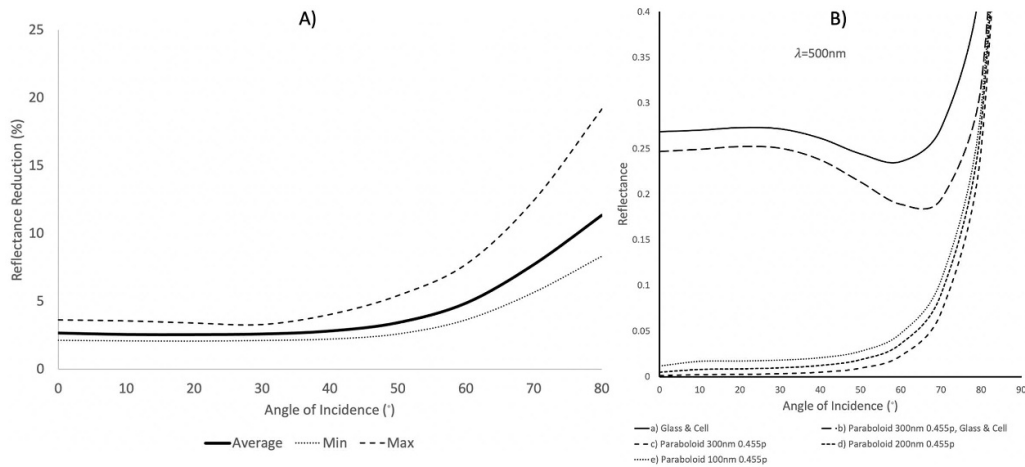| Angle of incidence (°)	Reflectance decrease		
	Min (%)	Max (%)	Avg (%)
0	2.12 (400 nm)	3.62 (300 nm)	2.67
10	2.08 (700 nm)	3.55 (300 nm)	2.56
20	2.06 (500 nm)	3.39 (300 nm)	2.55
30	2.11 (500 nm)	3.28 (300 nm)	2.60
40	2.21 (650 nm)	4.02 (350 nm)	2.82
50	2.59 (650 nm)	5.42 (350 nm)	3.43
60	3.64 (650 m)	7.72 (350 nm)	4.87
70	5.67 (600 nm)	12.45 (300 nm)	7.72
80	8.35 (800 nm)	19.19 (300 nm)	11.36

geometry replication. Increased porosity and refractive index gradient can be achieved by simple exposure to acidic solutions for some materials [9]. The relationship between purely porosity and optimum AR characteristics for PV (especially thin-film cells) is therefore required and presented in this work. This research helps distinguish between these two categories; AR effects due to porosity and specific nanostructure geometries, which are widely investigated and designed elsewhere.

FDTD involves more time and greater computational power, however, it has the capabilities to more accurately simulate actual geometries. Future work utilising FDTD would complete the comparison of geometry AR vs porosity AR. However, it should be noted that porous coatings for applications can still be based upon natural nanostructures, but focus on the porosity values those nanostructures produce. It has already been pointed out that very narrow structures are weaker, less durable and more challenging to manufacture. Decreasing the packing factor instead of specific nanostructures also results in less durable surface layers, hence focusing on the porosity may allow for more durable layering.

Schirone *et al* [9], applied porous Si on mono/multi-crystalline Si substrates via stain etching in aqueous HF/HNO$_3$ solutions. These AR coatings were found to reduce surface reflectance to $<3\%$ in the 400–800 nm wavelength range. Using etching processes or fabricating AR composite films are too expensive or not scaleable enough to be economically feasible according to more recent research [2]. Khan *et al* [2], therefore fabricated AR coatings in a high-vacuum e-beam evaporation system. Jang *et al* [4], also had nanostructures fabricated onto glass using this process. Here, the effective refractive index of the a-Si coating was controlled by the flux AOI.

The unconventional nanoimprint lithography (NIL) technique may be most promising for the coatings discussed in this study, due to its cost-effective and robust approach [12]. For example, Asadollahbaik *et al* [44], and Siddique *et al* [14], successfully fabricated regular Si moth-eye and irregular glass-wing butterfly nanostructures, respectively, using advanced etching techniques and NIL. Kuo *et al* [12], proposed a novel procedure for manufacturing a non-close-packed nanosphere monolayer, whereby an AR structure was replicated from

4.6. Practical solar cell application

The two main avenues for fabrication include accurately building the exact nanopattern geometries, or by building individual layers with separate refractive index values, much like how the optical model worked in this study. Taking individual layers with varying refractive indices seems like the logical solution to this problem, but how feasible is this on a large scale? An issue arises here when we consider the shortage of materials on Earth that have the specific refractive index values of each layer. To add to this, with each layer being $\sim$2–3 nm thick, it seems even more unlikely that this would be scaleable. To this end, the system could potentially be designed to have a gradual change in density/porosity that replicates this reduction in refractive index. This could be one of the easiest ways to construct AR coatings as it would require specific feature

Figure 8. (A) Average reflectance decrease for the a-Si thin-film system with the optimum AR coating, compared to just the a-Si thin-film system, at varied angles of incidence from $0°$ to $80°$. (B) Dependence of the reflection on AOI at $\lambda = 500$ nm for (a) glass and cell. (b) 300 nm, 15% spacing paraboloid nanostructure, glass and cell. (c) 300 nm, 15% spacing paraboloid nanostructure. (d) 200 nm, 15% spacing paraboloid nanostructure. (e) 100 nm, 15% spacing paraboloid nanostructure.

moth eye nanostructures onto a glass substrate by NIL. This method of fabrication is much cheaper than that for semiconductor coating and etching procedures. However, manufacturing techniques focused on purely varying the porosity of a materials outer layers are relatively underdeveloped [9]. Future work could use the NIL technique to replicate nanostructured geometry AR coatings and compare them with similar AR coatings that have the same refractive index gradient due to varying porosity. The cost, reflectance, estimated annual PV energy output and practicality of both types of AR can then all be compared.

To commercialise and apply the AR coatings to global solar industries, several issues must be tackled. This includes improvement of mechanical characteristics to withstand the external environment, fabrication simplification, durability and further reduction in costs [7, 45].

4.7. Limitations

The key observations and assumptions for the simulations of a-Si thin-film cells were based on simulations from the cone geometry only. There is a clear need for more initial simulations on a wider range of geometries to make more accurate initial assumptions (e.g. nipple spacing) and relate to porosity/refractive index gradients.

The number of effective refractive index layers allowed within the simulation software was limited to 100, but perhaps this is realistic due to the resolution limitations of nanostructure fabrication. There may also be errors associated with the exact Ray Tracing simulation layering, its accuracy in comparison to practical testing and the actual refractive indices used in this case study for a-Si with the specific thicknesses and refractive indices (table 2). Due to the comparative nature of the results taken, errors were consistent throughout this study and therefore offset all results by a constant amount, thus cancelling their effects out.
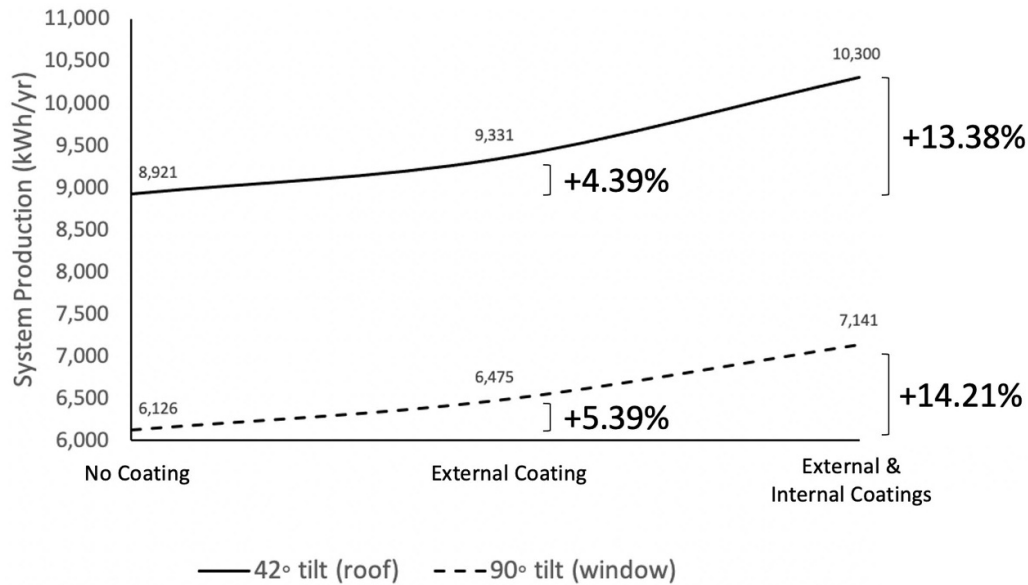
Table 4. Average reflectance between the 300–800 nm wavelength range, of an a-Si thin-film system for three cases: (1) without an AR coating, (2) using the optimum AR coating from this study between the glass and a-Si layers, (3) using the optimum AR coating from this study between the glass and a-Si layers in addition to the AR coating constructed by Jang *et al* [4], placed between the a-Si and ITO layers.

Angle of incidence (°)	Reflectance (%)		
	No coating	External coating	External and internal coatings
0	20.10	17.43	7.73
10	20.13	17.58	8.04
30	20.19	17.59	8.68
40	20.11	17.30	8.89
50	20.36	16.93	8.86
60	22.11	17.24	9.62
70	27.89	20.17	13.46
80	44.75	33.39	27.57

5. Recommendations and future directions

The AR Paraboloid geometry, with a nipple height of 300 nm and a nipple spacing of 15% (relative to the height), would create the optimal nanostructure for use on a-Si thin-film cells, within this study's investigations. In order to determine the optimal method of replicating the designed nanopatterns, it would be beneficial to compare these design pathways; as the exact nipple-shaped geometries, or as separate layers with varying densities to create the required refractive index gradient.

Simulations must now be performed on actual nm-scale nipple geometries, instead of the smooth layers with gradients of refractive indices used in this study. Future research could include multiple simulation methods to improve the robustness of the results, as each technique offers variations in capabilities and limitations [16]. FDTD is used to accurately simulate

Figure 9. Annual energy output of an a-Si thin-film system at 42° and 90° tilts for three cases, using PVSyst: (1) without an AR coating, (2) using the optimum AR coating from this study between the glass and a-Si layers, (3) using the optimum AR coating from this study between the glass and a-Si layers in addition to the AR coating constructed by Jang *et al* [4], placed between the a-Si and ITO layers.

actual geometry structures robustly, instead of smooth surfaces, hence this is recommended as an important technique to use in future work, despite downsides of requiring vastly more computational power and time.

It would be advisable to focus on a wider range of nipple spacings with AOI experiments performed on each, to replicate the glass wing structures and to understand their properties. The simulations in this study showed that data for varied angles of incidence can differ dramatically from the 0° data, in terms of how favourable it is compared to other geometries.

The data suggests that nipple height plays a more significant role than the precise geometry of the AR coatings in dictating reflections, in agreeance with research by Yoshida *et al* [22]. Due to the EMT method utilised, it is evident that the porosity and final refractive index for a layer has the dominating effect on reflectance.

There is clear potential for the use of multiple AR coatings on thin-film cells to increase reflectance at the higher wavelength values towards the infrared end of the spectrum, and to decrease reflectance for the smaller wavelengths. Coatings with different properties could be set in front of glass and between glass/ITO/a-Si layers. For example, AR coatings with the same refractive index gradient but with one using the specific geometry and the other varying in porosity.

6. Conclusion

The optimum geometry from this investigation was found to be the paraboloid structure. It was found that this AR paraboloid geometry nanostructure, with a nipple height of 300 nm and a nipple spacing of 15% relative to the height, gives the lowest reflectance values over a wider range of angles of incidence, when attached to an a-Si thin-film system. A small refractive index 'step' is required to aid total internal reflections and hence light trapping, which improves total energy absorption, hence justifying the non-zero optimum nipple spacing. When compared to the Solar System without the AR coating, this nanostructure reduced reflectance in the 300–800 nm wavelength range by an average of 2.665% at 0°, through to 11.36% at 80°, showing great wide angle capabilities. The largest reflection reduction was found to be 19.192% for $\lambda = 300$ nm and an AOI of 80°. These reductions, especially at greater angles of incidence, show great promise for the performance enhancement of commercial solar PV, where light from the Sun is incident from every angle throughout the day. This specific feature could have huge positive implications for morning and evening electricity production.

This AR coating has a greater reflection reduction at the lower end of the spectrum, whilst there is a smaller reflection reduction at the infrared end of the spectrum towards $\lambda = 800$ nm. This is an important property of this bio-inspired structure, whereby the efficiency of the a-Si cell will increase but not with the added defects caused by increased temperature from harmful infrared radiation. Solar cell performance would therefore increase proportionally to the decrease in reflection, due to the improved uptake of lower wavelength radiation.

The annual energy increase of the thin-film system was found to be 4.39% and 5.39% for 42° (standard UK roof) and 90° (vertical window) tilts, respectively, with the use of this study's optimum coating. Through use of two AR coatings, set between the glass, a-Si and ITO layers, the annual energy production was observed to increase by 13.38% and 14.21% for the 42° and 90° tilts, respectively. This demonstrates significant evidence for the capabilities of multiple AR coatings, to greatly enhance solar cell performance.

Data availability statement

The data that support the findings of this study are available upon reasonable request from the authors.

ORCID iDs

Timothy Pickering ⬤ https://orcid.org/0000-0002-6245-7714
Katie Shanks ⬤ https://orcid.org/0000-0002-6645-0181

References

[1] Department for Business, Energy & Industrial Strategy 2020 Solar photovoltaics deployment (National Statistics)

[2] Khan S B, Irfan S, Zhuanghao Z and Lee S L 2019 Influence of refractive index on antireflectance efficiency of thin films *Materials* **12** 1483

[3] Rayleigh L 1879 On reflection of vibrations at the confines of two media between which the transition is gradual *Proc. London Math. Soc.* **s1–11** 51–56

[4] Jang S J, Song Y M, Yeo C I, Park C Y, Yu J S and Lee Y T 2011 Antireflective property of thin film a-Si solar cell structures with graded refractive index structure *Opt. Express* **19** A108

[5] Stavenga D G, Foletti S, Palasantzas G and Arikawa K 2006 Light on the moth-eye corneal nipple array of butterflies *Proc. R Soc.* B **273** 661–7

[6] Darwin C 1859 *On the Origin of Species by Means of Natural Selection, or, The Preservation of Favoured Races in the Struggle for Life* (London: John Murray)

[7] Raut H K, Ganesh V A, Nair A S and Ramakrishna S 2011 Anti-reflective coatings: a critical, in-depth review *Energy Environ. Sci.* **4** 3779–804

[8] Schirone L, Sotgiu G, Rallo F and Califano F P 1996 Porous-silicon coatings for photovoltaic devices *Nuovo Cimento* D **18** 1225–32

[9] Schirone L, Sotgiu G and Califano F P 1997 Chemically etched porous silicon as an anti-reflection coating for high efficiency solar cells *Thin Solid Films* **297** 296–8

[10] Lehmann V and Gösele U 1991 Porous silicon formation: a quantum wire effect *Appl. Phys. Lett* **58** 856

[11] Breault R O 2006 Scattered light *Technical Report* (Breault)

[12] Kuo W-K, Hsu J-J, Nien C-K and Her Yu H 2016 Moth-eye-inspired biophotonic surfaces with antireflective and hydrophobic characteristics *ACS Appl. Mater. Interfaces* **8** 32021–30

[13] Edgehog 2018 Bio-inspired subwavelength nanostructures for antireflection *Technical Report* (Edgehog)

[14] Siddique R H, Gomard G and Hölscher H 2015 The role of random nanostructures for the omnidirectional anti-reflection properties of the glasswing butterfly *Nat. Commun.* **6** 1–8

[15] Han Z, Jiao Z, Niu S and Ren L 2019 Ascendant bioinspired antireflective materials: opportunities and challenges coexist *Progress Science Materials* **103** 1–68

[16] Han K and Chang C-H 2014 Numerical modeling of sub-wavelength anti-reflective structures for solar module applications *Nanomaterials* **4** 87–128

[17] Bernhard C G, Miller W H and Corneal Nipple A 1962 Pattern in insect compound eyes *Acta Physiol. Scand.* **56** 385–6

[18] Han Z W, Wang Z, Feng X M, Li B, Mu Z Z, Zhang J Q, Niu S C and Ren L Q 2016 Antireflective surface inspired from biology: a review *Biosurf. Biotribol.* **2** 137–50

[19] Bernhard C G, Gemne G and Sällström J 1970 Comparative ultrastructure of corneal surface topography in insects with aspects on phylogenesis and function *Z. Vergleichende Physiol.* **67** 1–25

[20] Lee K C, Yu Q and Erb U 2016 Mesostructure of ordered corneal nano-nipple arrays: the role of 5–7 coordination defects *Nat. Sci. Rep.* **6** 28324

[21] Spalding A, Shanks K, Bennie J, Potter U, Ffrench-Constant R, Modelling O and 2019 Phylogenetic analysis provide clues to the likely function of corneal nipple arrays in butterflies and moths *Insects* **10** 262

[22] Yoshida A, Motoyama M, Kosaku A and Miyamoto K 1997 Antireflective nanoprotuberance array in the transparent wing of a hawkmoth, cephonodes hylas *Zool. Sci.* **14** 737–41

[23] Boden S A and Bagnall D M 2006 Bio-mimetic subwavelength surfaces for near-zero reflection sunrise to sunset *Conf. Record of the 2006 IEEE 4th Conf. on Photovoltaic Energy Conversion, WCPEC-4* vol 2 pp 1358–61

[24] Chen J D, Zhou L, Ou Q D, Li Y Q, Shen S, Lee S T and Tang J X 2014 Enhanced light harvesting in organic solar cells featuring a biomimetic active layer and a self-cleaning antireflective coating *Adv. Energy Mater.* **4** 1301777

[25] Forberich K, Dennler G, Scharber M C, Hingerl K, Fromherz T and Brabec C J 2008 Performance improvement of organic solar cells with moth eye anti-reflection coating *Thin Solid Films* **516** 7167–70

[26] Yeol Yoo G, Nurrosyid N, Lee S, Jeong Y, Yoon I, Kim C, Kim W, Jang S-Y and Rag Do Y 2020 Newly developed broadband antireflective nanostructures by coating a low-index MgF$_2$ film onto a SiO$_2$ moth-eye nanopattern *ACS Appl. Mater. Interfaces* **12** 10626–36

[27] Wang C, Meng F, Wu M, Lin X, Wang T, Qiu J and Ma T 2013 A low-cost bio-inspired integrated carbon counter electrode for high conversion efficiency dye-sensitized solar cells *Phys. Chem. Chem. Phys.* **15** 14182–7

[28] Yu P, Chiu M-Y, Chang C-H, Hong C-Y, Tsai Y-L, Han H-V and Wu Y-R 2014 Towards high-efficiency multi-junction solar cells with biologically inspired nanosurfaces *Prog. Photovolt., Res. Appl.* **22** 300–7

[29] Leem J W, Su Yu J, Jun D H, Heo J and Park W K 2014 Efficiency improvement of III–V GaAs solar cells using biomimetic TiO$_2$ subwavelength structures with wide-angle and broadband antireflection properties *Sol. Energy Mater. Sol. Cells* **127** 43–49

[30] Siddique R H, Donie Y J, Gomard G, Yalamanchili S, Merdzhanova T, Lemmer U and Hölscher H 2017 Bioinspired phase-separated disordered nanostructures for thin photovoltaic absorbers *Sci. Adv.* **3** e1700232

[31] Badri S H and Gilarlue M M 2020 Silicon nitride waveguide devices based on gradient-index lenses implemented by subwavelength silicon grating metamaterials *Appl. Opt.* **59** 5269

[32] Badri S H and Gilarlue M M 2019 Low-index contrast waveguide bend based on truncated Eaton lens implemented by graded photonic crystals *J. Opt. Soc. Am.* B **36** 1288–93

[33] Bruggeman D A 1935 Berechnung verschiedener physikalischer Konstanten von heterogenen Substanzen. I. Dielektrizitätskonstanten und Leitfähigkeiten der Mischkörper aus isotropen Substanzen *Ann. Phys., Lpz.* **416** 636–64

[34] Choy T C 2016 *Effective Medium Theory: Principles and Applications* (New York: Oxford University Press)

[35] Vogt K 1974 Optische Untersuchungen an der Cornea der Mehlmotte Ephestia kühniella *J. Comp. Physiol.* **88** 201–16

[36] Cai J and Qi L 2015 Recent advances in antireflective surfaces based on nanostructure arrays *Mater. Horiz.* **2** 37–53

[37] Schott 2019 Optical glass data sheets *Technical Report* (SCHOTT)

[38] König T A F, Ledin P A, Kerszulis J, Mahmoud M A, El-Sayed M A, Reynolds J R and Tsukruk V V 2014 Electrically tunable plasmonic behavior of nanocube–polymer nanomaterials induced by a redox-active electrochromic polymer *ACS Nano* (https://doi.org/10.1021/nn501601e)

[39] Richter A, Glunz S and Benick J 2008 Spectral ellipsometry analysis of ultrathin amorphous silicon layers *European Photovoltaic Solar Conf. and Exhibition*

[40] OCD Applications 2015 Product overview n&k OptiPrime-TF *Technical Report* (n&k Technology)

[41] Shamiryan D and Dmitriy V 2012 Spectroscopic ellipsometry of ion-implantation-induced damage *Ion Implantation* (Rijeka: InTech)

[42] Johnson P B and Christy R W 1972 Optical constants of the noble metals *Phys. Rev.* B **6** 4370–9

[43] Rahman A, Ashraf A, Xin H, Tong X, Sutter P, Eisaman M D and Black C T 2015 Sub-50-nm self-assembled nanotextures for enhanced broadband antireflection in silicon solar cells *Nat. Commun.* **6** 1–6

[44] Asadollahbaik A, Boden S A, Charlton M D B, Payne D N R, Cox S and Bagnall D M 2014 Reflectance properties of silicon moth-eyes in response to variations in angle of incidence, polarisation and azimuth orientation *Opt. Express* **22** A402

[45] Choi H-J, Huh D, Jun J and Lee H 2019 A review on the fabrication and applications of sub-wavelength anti-reflective surfaces based on biomimetics *Appl. Spectrosc. Rev.* **54** 719–35